

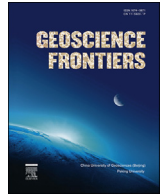
HOSTED BY



Contents lists available at ScienceDirect

China University of Geosciences (Beijing)

Geoscience Frontiers

journal homepage: www.elsevier.com/locate/gsf

Research paper

The origin of high eccentricity planets: The dispersed planet formation regime for weakly magnetized disks

Yusuke Imaeda*, Toshikazu Ebisuzaki

RIKEN, 2-1, Hirosawa, 351-0198, Japan

ARTICLE INFO

Article history:

Received 8 April 2016

Received in revised form

1 July 2016

Accepted 6 July 2016

Available online xxx

Keywords:

Accretion disk

Planet formation

Magnetorotational instability

ABSTRACT

In the tandem planet formation regime, planets form at two distinct sites where solid particles are densely accumulated due to the on/off state of the magnetorotational instability (MRI). We found that tandem planet formation can reproduce the solid component distribution of the Solar System and tends to produce a smaller number of large planets through continuous pebble flow into the planet formation sites. In the present paper, we investigate the dependence of tandem planet formation on the vertical magnetic field of the protoplanetary disk. We calculated two cases of $B_z = 3.4 \times 10^{-3}$ G and $B_z = 3.4 \times 10^{-5}$ G at 100 AU as well as the canonical case of $B_z = 3.4 \times 10^{-4}$ G. We found that tandem planet formation holds up well in the case of the strong magnetic field ($B_z = 3.4 \times 10^{-3}$ G). On the other hand, in the case of a weak magnetic field ($B_z = 3.4 \times 10^{-5}$ G) at 100 AU, a new regime of planetary growth is realized: the planets grow independently at different places in the dispersed area of the MRI-suppressed region of $r = 8\text{--}30$ AU at a lower accretion rate of $M < 10^{-7.4} M_\odot \text{ yr}^{-1}$. We call this the “dispersed planet formation” regime. This may lead to a system with a larger number of smaller planets that gain high eccentricity through mutual collisions.

© 2016, China University of Geosciences (Beijing) and Peking University. Production and hosting by Elsevier B.V. This is an open access article under the CC BY-NC-ND license (<http://creativecommons.org/licenses/by-nc-nd/4.0/>).

1. Introduction

A star is born together with the planets orbiting around it from the gravitational collapse of a dense core of a molecular cloud (e.g., [Bouvier et al., 2007](#)). This collapse produces a centrifugally supported thin disk around the protostar, and the solid particles grow from the submicron scale to the order of 10^4 km in the disk. Recent observations have shown that planets can be found around stars universally, and the number of confirmed exoplanets is 2107 as of April 2016 (<http://exoplanet.eu/catalog/>). Many of the exoplanets, however, do not resemble the planets in our Solar System. For example, some exoplanets have large orbital eccentricities and are called eccentric planets ([Marcy and Butler, 1996](#)).

Theoretically, planet formation has also been investigated by many researchers since the early 1970s, and the core accretion model has been proposed as a formation scenario for planets. In the classical core accretion model, planetesimals form first; these are solid bodies on the order of 10 km. They are produced by the gravitational instability of the particle layer (e.g., [Safronov, 1969](#);

[Goldreich and Ward, 1973](#); [Hayashi et al., 1985](#)) or the mutual sticking of particles ([Weidenschilling, 1977a](#); [Weidenschilling and Cuzzi, 1993](#)). After planetesimals form, they coagulate with each other, which leads to runaway growth ([Wetherill and Stewart, 1989](#)) and then oligarchic growth ([Kokubo and Ida, 1998](#)) until they reach the isolation masses to form the planetary core. If this core reaches the critical core mass (i.e., several Earth masses) before the gas depletion of the protoplanetary disk, it rapidly attracts the surrounding gas and becomes a gas or icy giant (e.g., [Mizuno, 1980](#); [Pollack et al., 1996](#)). Otherwise, it remains a terrestrial planet.

The classical core accretion model had three difficulties: the formation timescale problem, dust fragmentation and infall problem, and planet migration problem. Nevertheless, recent investigations have gradually solved these difficulties. First, the formation timescale problem was overcome by pebble accretion ([Johansen et al., 2006, 2007](#); [Johansen and Youdin, 2007](#); [Johansen et al., 2009, 2011](#); [Johansen and Lacerda, 2010](#); [Ormel and Klahr, 2010](#); [Lambrechts and Johansen, 2012, 2014](#)). The particle growth by pebble capturing accelerates the planetary growth. Second, the dust fragmentation and infall problem was eluded by the introduction of the porous nature of icy particles beyond the snowline. Although meter-sized compact particles are selectively lost from the disk by radial infall (~ 1000 yrs), the particles can quickly grow

* Corresponding author.

E-mail address: yusuke.imaeda@riken.jp (Y. Imaeda).

Peer-review under responsibility of China University of Geosciences (Beijing).

<http://dx.doi.org/10.1016/j.gsf.2016.07.001>1674-9871/© 2016, China University of Geosciences (Beijing) and Peking University. Production and hosting by Elsevier B.V. This is an open access article under the CC BY-NC-ND license (<http://creativecommons.org/licenses/by-nc-nd/4.0/>).

as large as the mean free path of the gas molecule if the porous aggregation is considered in the icy region ($T_m < 150$ K). This changes the gas drag law on the particles from the Epstein regime to the Stokes regime, which eventually terminates the radial drift of a particle when its mass reaches $\sim 10^{10}$ g (Okuzumi et al., 2012). Therefore, the dust infall problem in the classical model has been partially overcome, although the problem still remains in the rocky region ($T_m > 150$ K). Furthermore, the reduction of the relative particle–particle velocity also mitigates the fragmentation problem. Third, the planet migration problem was solved by introducing the dynamic term of the corotation torque. The gravitational interaction between the planet and gas disk causes planetary migration over a short timescale, but introducing the dynamic term in the torque formula reduces the inward migration rate considerably (Paardekooper, 2014; Sasaki and Ebisuzaki, 2016).

Motivated by the recent progress in planet formation theory, we (Ebisuzaki and Imaeda, 2016, hereafter paper I) constructed a steady-state one-dimensional model of the accretion disk around a protostar based on the α -model of an accretion disk according to the standard formulation of Shakura and Sunyaev (1973) and Lynden-Bell and Pringle (1974). We further investigated the particle evolution within this disk. In order to construct the disk model, we considered the magnetorotational instability (MRI) (Balbus and Hawley, 1991; Hawley and Balbus, 1991), layered accretion (Gammie, 1996), and ionization due to the galactic cosmic rays and radioactive nuclei (Umebayashi and Nakano, 1988). The ionization due to thermal collision (Balbus and Hawley, 2000) was also considered as the ionization source. For the particle evolution, we considered porous aggregation and compaction (Okuzumi et al., 2012; Kataoka et al., 2013).

We found that the disk is divided into three regions by two distinct locations: the outer MRI front at r_{out} and the inner MRI front at r_{in} ; these locate around $7 \text{ AU} \leq r_{out} \leq 60 \text{ AU}$ and $0.2 \text{ AU} \leq r_{in} \leq 1 \text{ AU}$, respectively (see Fig. 1a). First, outside the outer MRI front, MRI takes place, and the disk is turbulent because of the

ionization due to the galactic cosmic rays (Umebayashi and Nakano, 1988). Second, between the two MRI fronts, no MRI occurs around the midplane (MRI-suppressed region) (e.g., Sano and Miyama, 1999; Sano et al., 2000). This turbulent-free area is sandwiched by two turbulent surface layers (i.e., turbulent envelopes), where the ionization degree is high enough to activate MRI (Gammie, 1996). Third, inside the inner MRI front (inner turbulent region: ITR), MRI takes place due to the thermal ionization of K and Na (Balbus and Hawley, 2000). This corresponds to the location where the disk temperature is $T_m = 1000\text{--}1300$ K. Finally, the disk is truncated by the stellar magnetic field at the Alfvén radius ($0.01 \text{ AU} \leq r_A \leq 0.04 \text{ AU}$). This three-region structure is consistent with the recent comprehensive review by Armitage (2011).

We further investigated the particle drift and sedimentation to the midplane in the disk (Nakagawa et al., 1986). In contrast to the classical core accretion model, we considered both the particle growth by mutual sticking with porosity evolution (Okuzumi et al., 2012; Kataoka et al., 2013) and the gravitational instability of the particle sub-disk (Yamato and Sekiya, 2004). As a result, the gravitational instability takes place after the particles are completely decoupled from the turbulent gas. This is different from the classical view, where the gravitational instability takes place during the partial decoupling stage, and may be significant to avoiding the dust infall problem. Such a late-stage gravitational instability was reported by Carballido et al. (2006) to explain the formation of the Kuiper belt objects.

In paper I, we showed that planet formation is restricted to two distinct sites in the disk: around the outer MRI front and the inner MRI front. At the outer MRI front, porous icy aggregates grow (Okuzumi et al., 2012; Kataoka et al., 2013) and are subjected to the gravitational instability of the particle sub-disk to make the planetesimals (Yamato and Sekiya, 2004). Then, they finally reach 10^{27} g $\sim M_{\oplus}$ within a million years to become icy planets or gas giant cores. On the other hand, volatile-free rocky planetesimals form around the inner MRI front because the distraction associated

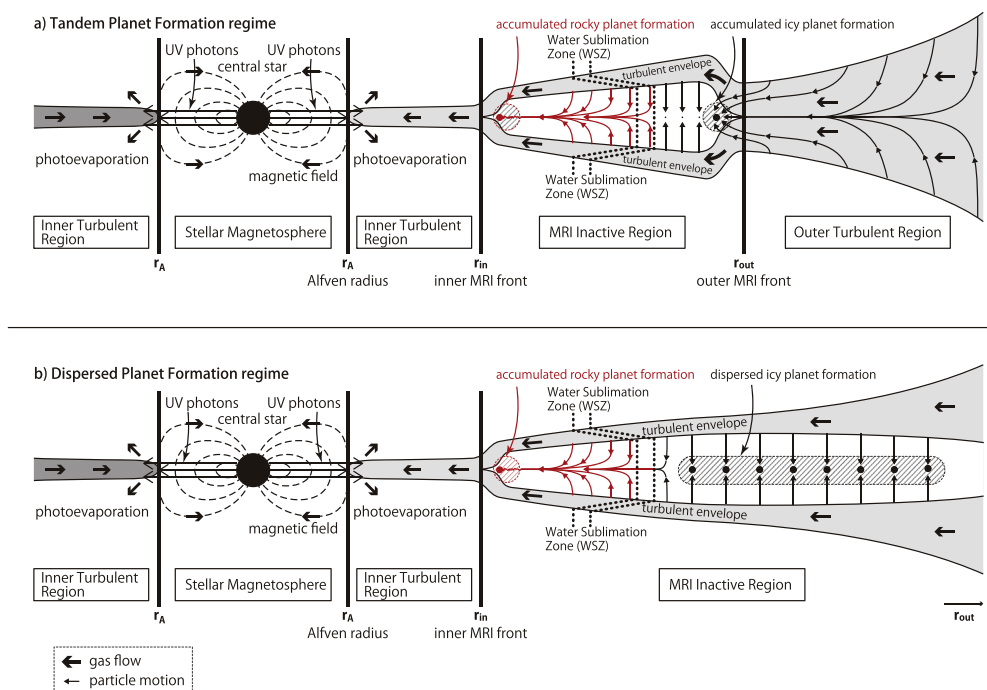


Figure 1. Schematic cross-section of the two regimes of planet formation. (a) Tandem planet formation regime: Planet formation is strictly restricted around two sites: the outer and inner MRI fronts. Continuous pebble supplied by the particle drift to the sites sustains the rapid growth of planets at these locations. (b) Dispersed planet formation: Icy planet formation is dispersed to the entire region of the disk outside the snowline (WSZ), although the same rocky planet formation takes place at the inner MRI front.

with high-speed particle–particle collision prohibits the growth of particles more massive than a pebble of $\sim 10^4$ g when the disk temperature is higher than the H_2O sublimation temperature, i.e., $T_m > 180$ K. As a result, particles around the inner MRI front lose the volatile component completely before they arrive there and become volatile-free. Then, the accumulated pebbles are subjected to gravitational instability to form kilometer-sized planetesimals (Chatterjee and Tan, 2014, 2015) and grow further by pebble accretion (e.g., Johansen et al., 2006) to form the planet mass object.

In summary, we successfully constructed a quantitative model of planetesimal formation in the $\dot{M} = 10^{-7.0} M_\odot \text{ yr}^{-1}$ disk and named it the tandem planet formation regime because there are two distinct sites of planetary formation in the disk.

Then, we (Imaeda and Ebisuzaki, 2016, hereafter paper II) investigated how planetary formation proceeds in a disk with various accretion rates in the range of $\dot{M} = 10^{-8.0} - 10^{-6.5} M_\odot \text{ yr}^{-1}$.

In the present paper, we further examine the dependence of the tandem planet formation on the vertical magnetic field. This is because the location of the MRI fronts, which is a key parameter in tandem planet formation, strongly depends on the vertical magnetic field through the Elsasser number Λ (see the next section for details). The strength of the magnetic field at the 1000–10,000 AU scale is on the order of $10^{-3} - 10^{-5}$ G based on molecular cloud observations (Crutcher et al., 2010). The strength of the magnetic field at 100 AU should be considerably but not so much larger than the values in the dense core of the molecular cloud because the contracting gas partially drags a magnetic flux in 100 AU scale.

In Section 2, therefore, we present two cases of $B_z = 3.4 \times 10^{-3}$ G and $B_z = 3.4 \times 10^{-5}$ G at 100 AU as well as the canonical case of $B_z = 3.4 \times 10^{-4}$ G. In Section 3, we investigate the particle growth and planet formation in such strongly and weakly magnetized disks. We found that the tandem planet formation regime holds up well in the case of the strong magnetic field ($B_z = 3.4 \times 10^{-3}$ G). On

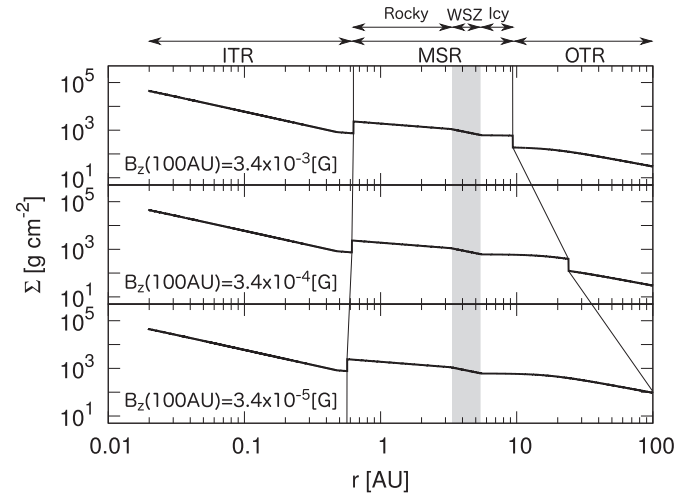


Figure 3. Column density distribution of the gas disk, where the accretion rate is $10^{-7.0} M_\odot \text{ yr}^{-1}$ with different $B_z(100\text{AU})$.

the other hand, in the case of a weak magnetic field ($B_z = 3.4 \times 10^{-5}$ G at 100 AU), a new regime of planetary growth takes place: the planets grow independently at different places in the dispersed area of the MRI-suppressed region (MSR) ($r = 8 - 30$ AU) when the accretion rate is as small as $\dot{M} < 10^{-7.4} M_\odot \text{ yr}^{-1}$. We call this formation mode “dispersed planet formation”, and consider as the possible origin of the eccentric planets. In Section 4, we discuss this new planet formation mode and contrast it with the tandem planet formation regime. Finally, we summarize our conclusions in Section 5.

2. Structure of a gas disk with different magnetic fields

2.1. Numerical method to construct the gas disk

The gas disk model constructed in paper I is based on the one-dimensional steady disk model formulated by Shakura and Sunyaev (1973) and Lynden-Bell and Pringle (1974). The accretion rate of the disk onto the central star \dot{M} and the vertically integrated column density Σ are related as follows:

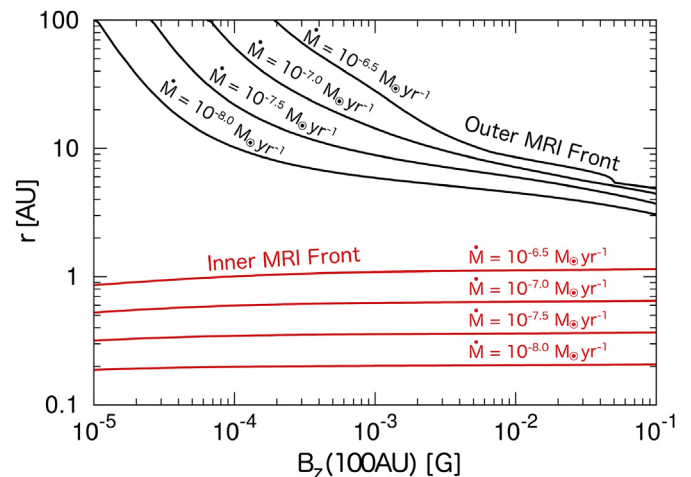


Figure 4. Locations of the outer (black) and inner (red) MRI fronts plotted against $B_z(100\text{AU})$ for various accretion rates of $\dot{M} = 10^{-6.5}, 10^{-7.0}, 10^{-7.5}, 10^{-8.0} M_\odot \text{ yr}^{-1}$. The other parameters are the same as those in paper I, where the canonical model is $B_z(100\text{AU}) = 3.4 \times 10^{-4}$ G and $\dot{M} = 10^{-7.0} M_\odot \text{ yr}^{-1}$.

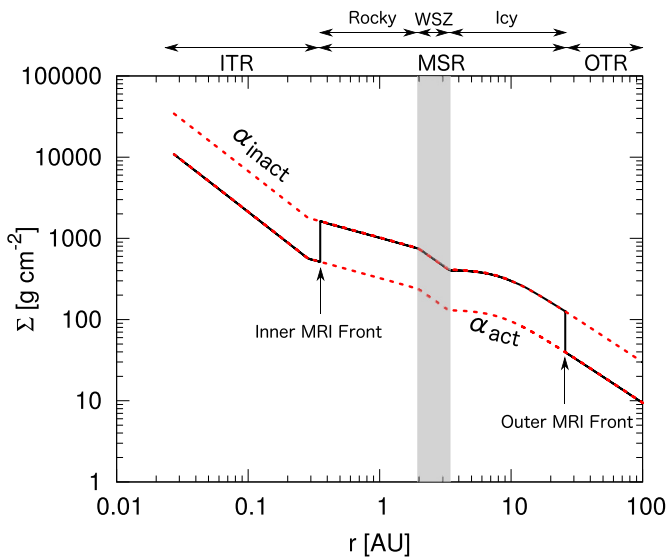


Figure 2. The column density of the disk model (black curve) comprises two steady disk solutions. The canonical case in paper I is shown, where the strength of the magnetic field is $B_z(100\text{AU}) = 3.4 \times 10^{-4}$ G and the accretion rate is $\dot{M} = 10^{-7.0} M_\odot \text{ yr}^{-1}$. The upper and lower red dotted curves represent the solutions of the MRI-inactive disk with $\alpha_{\text{inact}} = 10^{-2.5}$ and MRI-active disk with $\alpha_{\text{inact}} = 10^{-2.0}$, respectively. At the outer and inner MRI fronts, the Elsasser number is unity (i.e., $\Lambda = 1$) in the $\bar{\alpha} = \alpha_{\text{act}}$ disk. They divide the disk into the outer turbulent region (OTR), MRI-suppressed region (MSR), and inner turbulent region (ITR) from the outside inward. The MSR is further subdivided into the icy MSR, water sublimation zone (WSZ), and rocky MSR. When we alter the magnetic field strength, the locations of the MRI fronts shift to the new $\Lambda = 1$ position in the same $\bar{\alpha} = \alpha_{\text{act}}$ disk.

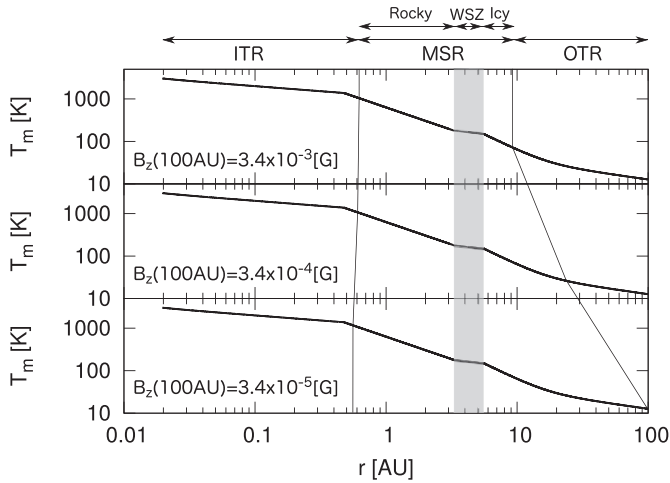


Figure 5. Temperature distribution of the gas disk with different $B_z(100\text{AU})$.

The gas disk is constructed by using two steady-state disk models: an MRI-active disk with $\alpha_{\text{act}} = 10^{-2.0}$ and MRI-inactive disk with $\alpha_{\text{inact}} = 10^{-2.5}$. When the Elsasser number Λ is larger than unity, MRI takes place, and the disk becomes turbulent and viscous (e.g. Jin, 1996; Sano and Miyama, 1999; Sano et al., 2000; Turner et al., 2007). In such a case, we select the MRI-active solution with $\bar{\alpha} = \alpha_{\text{act}} = 10^{-2.0}$. Otherwise, we select the MRI-inactive solution with $\bar{\alpha} = \alpha_{\text{act}} = 10^{-2.5}$. The Elsasser number is defined as follows:

$$\Lambda = \frac{B_z^2}{4\pi\rho_m\eta_0\Omega} \quad (3)$$

where B_z is the vertical component of the magnetic field and η_0 is the ohmic resistivity given by (e.g. Turner et al., 2007):

$$\eta_0 = 234 T_m^{1/2} x_e^{-1} \quad (4)$$

In addition, ρ_m is the gas density at the midplane, and x_e is the ionization degree of the gas disk.

To obtain the distribution of the vertical magnetic field, the following differential equation is used:

$$\frac{d \ln B_z}{d \ln r} = -\frac{2}{1+D} \quad (5)$$

This is numerically solved by using the turbulent magnetic diffusion constant (Lazarian and Vishniac, 1999):

$$D = \frac{8}{3} \frac{\pi \xi}{\sqrt{\bar{\alpha}}} \frac{B_z r \Omega}{\sqrt{4\pi\rho_m c_s^2}} \quad (6)$$

where we adopt $\xi = 0.003$. We inwardly integrate equation (5) from the outer boundary at $r = 100 \text{ AU}$ to give $B_z(100 \text{ AU})$ as a free parameter of the model.

2.2. Results of the gas disk model

Figs. 2 and 3 show the column density distribution of the disk. In Fig. 2, the active disk ($\bar{\alpha} = \alpha_{\text{act}}$) and inactive disk ($\bar{\alpha} = \alpha_{\text{inact}}$)

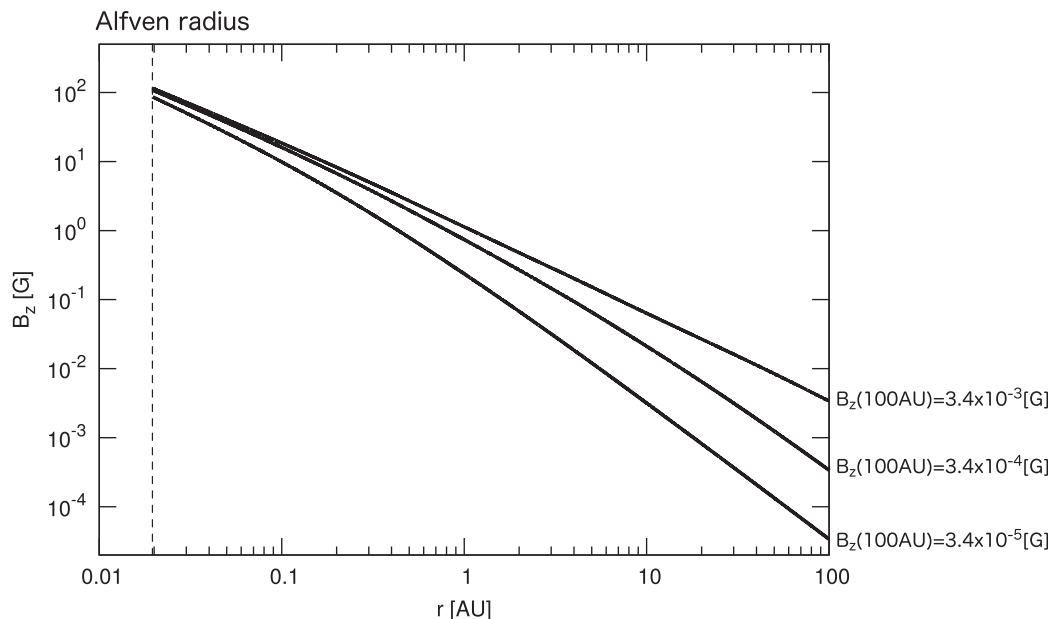


Figure 6. Distribution of the magnetic field for different $B_z(100\text{AU})$. The vertical magnetic fields asymptotically converge with each other to $\sim 100 \text{ G}$ toward the Alfvén radius.

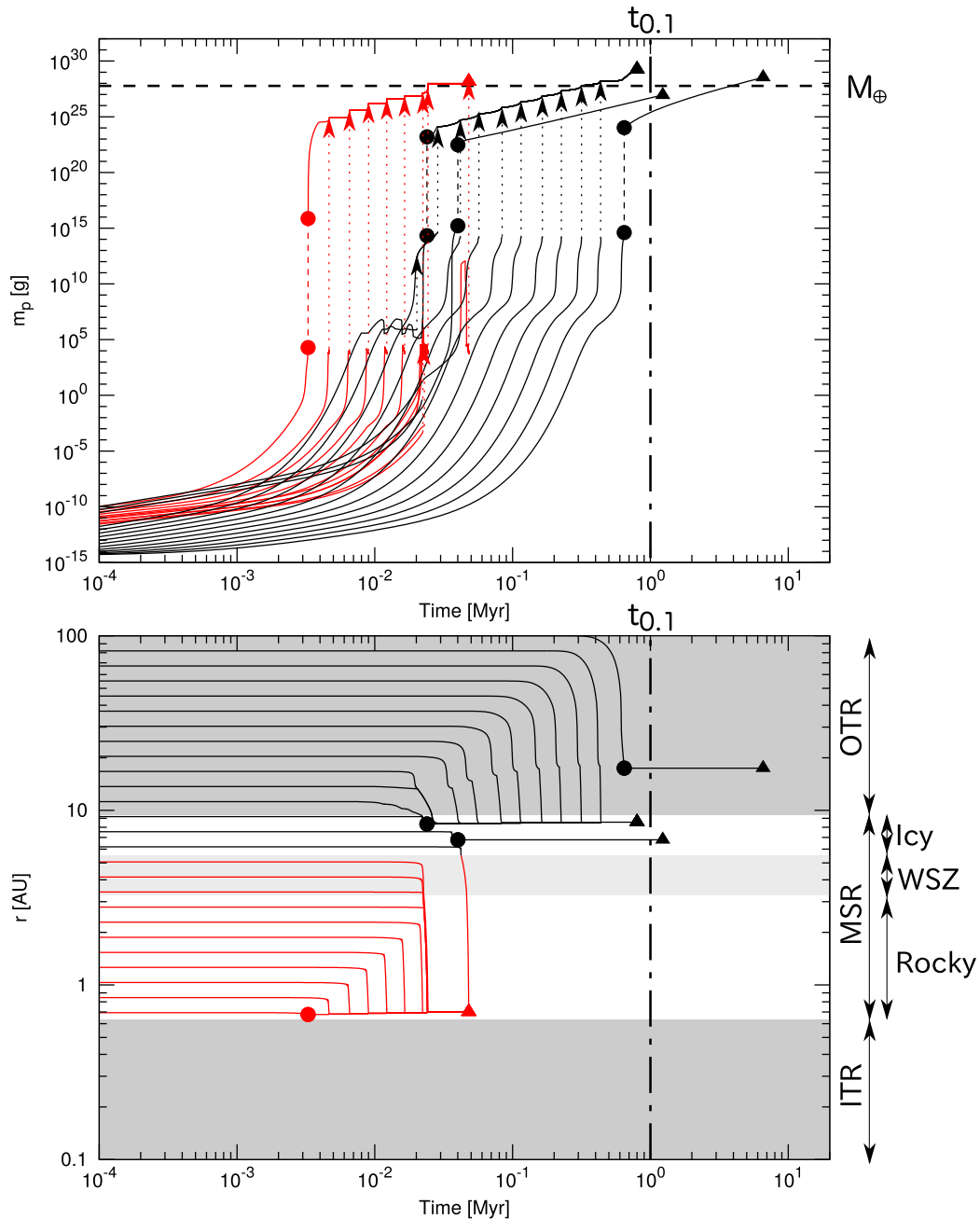


Figure 7. Particle evolution in the gas disk for $B_z(100\text{AU}) = 3.4 \times 10^{-3}$ G, which is 10 times stronger than the canonical value ($B_z(100\text{AU}) = 3.4 \times 10^{-4}$ G). Each line represents the particle trajectory on the t - m_p plane and t - r_p plane. The black color denotes particles in the icy region ($T_m < 150$ K), while the red color denotes particles in the rocky region ($T_m > 150$ K). The filled triangles represent the timing when the particles reach the final mass $m_f \equiv 2\pi r_p r_H \Sigma_p$, while the filled circles represent the timing when the gravitational instability of the particle sub-disk occurs. The vertical dashed lines in the upper panel represent the mass jump associated with the gravitational instability. The horizontal dashed line and vertical chain line represent the Earth mass M_\oplus and $t_{0.1} = 0.1M_\odot/\dot{M}$, respectively.

are represented by two red dashed lines, while the gas disk model is represented by a thin black line. The strength of the magnetic field and accretion rate are $B_z(100\text{AU}) = 3.4 \times 10^{-4}$ G and $\dot{M} = 10^{-7.0} M_\odot \text{ yr}^{-1}$, respectively. Because the effect of the magnetic field is only included in the Elsasser number, the magnetic field acts only as the location controller of the MRI fronts. The inactive solution has a large column density compared to the active solution, so the column density jump can be found in the disk model. The inactive part of the disk is called the MRI-suppressed region (MSR). This is further subdivided into three parts: the icy MSR, water sublimation zone (WSZ), and rocky MSR. The active part outside the WSZ is the outer turbulent

region (OTR), and that inside the MSR is the inner turbulent region (ITR). Therefore, the gas disk consists of three components: OTR, MSR, and ITR from outside inward. If we change $B_z(100\text{AU})$, this has no influence on the active and inactive solutions, only on the location of switching points. In other words, the MRI fronts shift inward or outward (Fig. 3).

To demonstrate these shifts clearly, Fig. 4 shows the locations of the MRI fronts as a function of $B_z(100\text{AU})$. The parameters are the same as those in paper I except for the strength of the magnetic field. The solid curves represent the locations of the MRI fronts. The upper black curves are the outer MRI fronts, and the lower red curves are the inner MRI fronts with various M . Because the

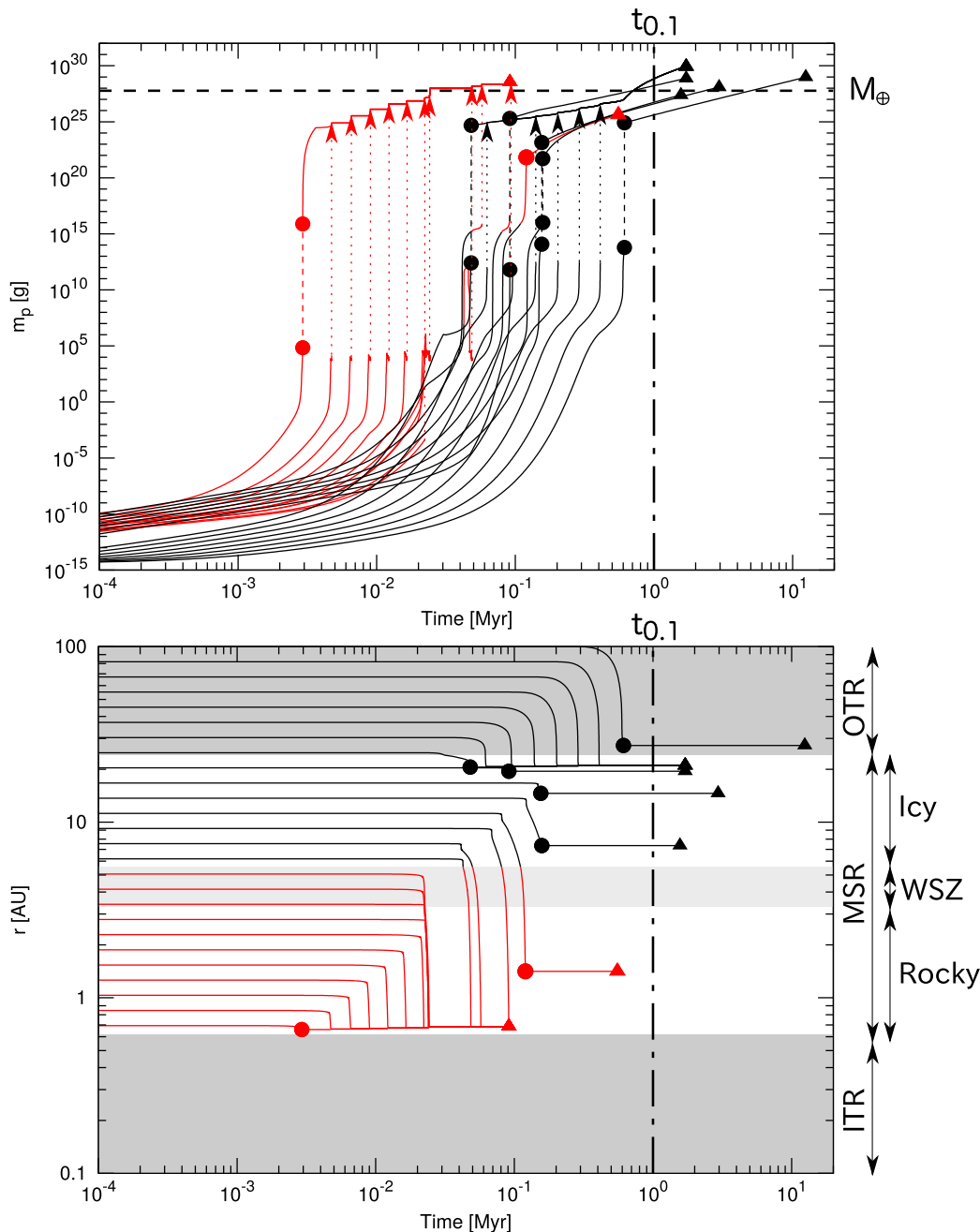


Figure 8. Same as Fig. 7 but for $B_z(100\text{AU}) = 3.4 \times 10^{-4}$ G.

maximum $B_z(100\text{AU})$ is not as large as $\sim 1\text{G}$ in reality, we can safely say that the disk models always have the MSR between the ITR and OTR. On the other hand, if the magnetic field is weak enough, the outer MRI front does not exist in 100AU. This occurs in the case of $B_z(100\text{AU}) \leq 6 \times 10^{-5}$ G for $\dot{M} = 10^{-7.0} M_\odot \text{yr}^{-1}$. We discuss the particle evolution in such a weak magnetic case in the next section.

Fig. 5 shows the temperature distribution of the gas disk with $\dot{M} = 10^{-7} M_\odot \text{yr}^{-1}$. Fig. 6 shows the magnetic field distribution obtained by solving equation (5). The magnetic fields of three cases with different $B_z(100\text{AU})$ asymptotically converge with each other to ~ 100 G toward the Alfvén radius (~ 0.02 AU) (Okuzumi et al., 2014). Considering the gas contraction from ~ 0.02 AU to the stellar surface, this magnetic field strength is consistent with observations in which the photospheric strength of the magnetic field of classical T Tauri stars is on the order of ~ 1 kG (Johns-Krull, 2007).

3. Particle evolution in the gas disk

3.1. Numerical method

We investigated the particle growth in the gas disk by considering the mutual coagulation, porosity evolution, and radial drift of particles. We also considered particle destruction by high-speed particle–particle collisions and the gravitational instability of the particle sub-disk. The particle coagulation equation is written as follows:

$$\dot{m}_p = \rho_p \pi a_p^2 \left(1 + \frac{v_{\text{esc}}^2}{v_{\text{rel,pp}}^2} \right) v_{\text{rel,pp}} \quad (7)$$

where m_p , ρ_p , a_p , v_{esc} , and $v_{\text{rel,pp}}$ are the particle mass, particle mass density in space, particle radius, escape velocity of a particle, and

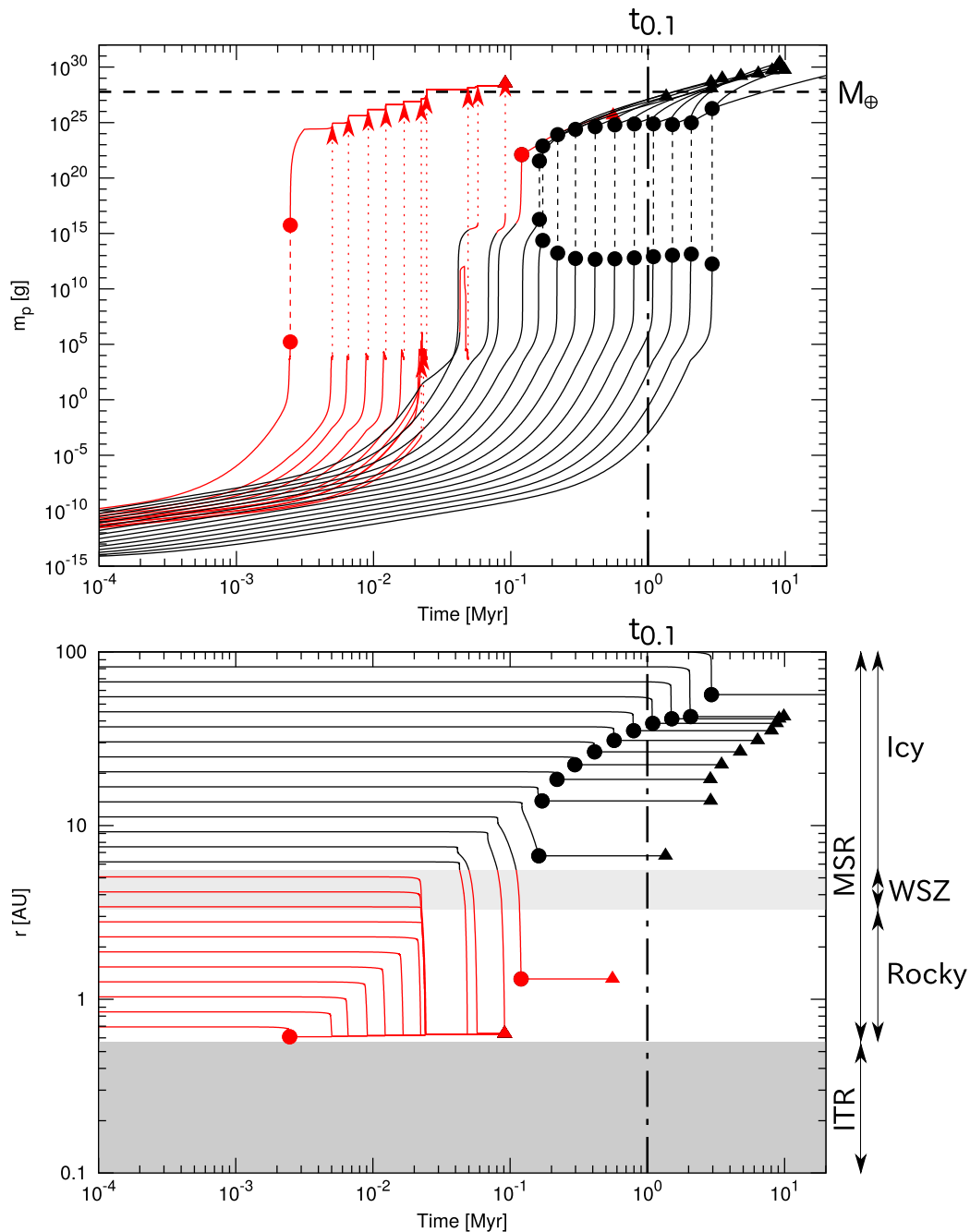


Figure 9. Same as Fig. 7 but for $B_z(100\text{AU}) = 3.4 \times 10^{-5}$ G, which is 0.1 times stronger than the canonical case.

relative velocity between particles, respectively. Here, many particles in a swarm are given a single representative mass for simplicity. Such simplification is justified by Sato et al. (2016), who compared the results with and without the mass distribution effect in their calculation. The particle mass density in space ρ_p is calculated from the particle disk scale height H_p of Youdin and Lithwick (2007), and the relative velocity between particles $v_{\text{rel,pp}}$ is obtained from Ormel and Cuzzi (2007). To calculate the particle radius, we considered the evolution of the particle internal density (or porosity) from Okuzumi et al. (2012) and Kataoka et al. (2013). The criterion for particle destruction by high-speed collision was taken from Stewart and Leinhardt (2009) and Wada et al. (2009).

We integrate the particle coagulation (Eq. (7)) in Lagrangian coordinates by using super-particles. A super-particle begins to

drift inward when its Stokes number is on the order of unity. The drift velocity was taken from Nakagawa et al. (1986). At the same time, the particles begin to concentrate on the midplane of the disk to form the particle sub-disk. When the gas density ρ_m and particle mass density in space ρ_p are comparable, the effect of particle stirring by the Kelvin–Helmholtz instability (KHI) can be considered. The strength of the viscosity induced by KHI turbulence was given by Takeuchi et al. (2012). Although KHI turbulence is thought to prevent the gravitational instability of the particle sub-disk, this turns out to not be necessarily true, particularly after the particles sufficiently grow and are decoupled from the gas. Indeed, they are decoupled from the gas. Hence the particle sub-disk is subjected to gravitational instability to form planetesimals.

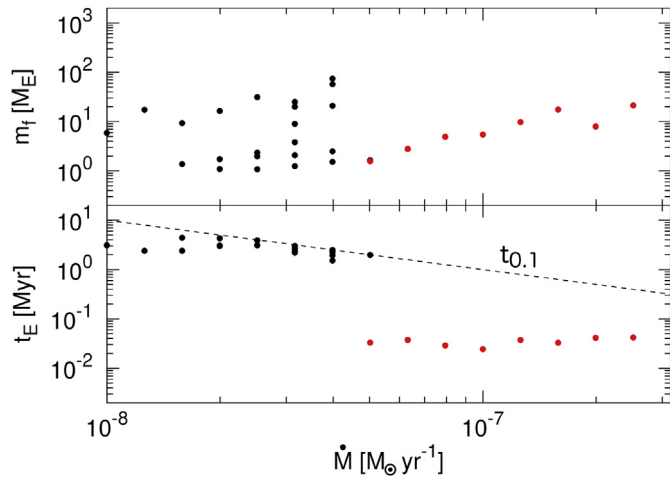


Figure 10. Time when the particle reaches 1 Earth mass M_{\oplus} (bottom panel) and the final mass of the particle, which is defined by $m_f = 2\pi r_p r_H \Sigma_p$ (top panel), as the function of the accretion rate. These were compiled from various cases with different accretion rates from $\dot{M} = 10^{-6.5} M_{\odot} \text{ yr}^{-1}$ down to $\dot{M} = 10^{-8.0} M_{\odot} \text{ yr}^{-1}$ with a difference of 0.1 Dex. The strength of the magnetic field was set to be $3.4 \times 10^{-5} \text{ G}$. The black points represent the particles in the icy region ($T_m < 150 \text{ K}$), while the red points are those in the rocky region ($T_m > 150 \text{ K}$). The dashed line is $t_{0,1}$, which indicates the limitation of the steady disk assumption in the gas disk. Therefore, only the points below the dashed line are plotted.

However, the assumption of a single representative mass is no longer valid after the planetesimal formation because runaway growth of the particles occurs. The runaway growth is later replaced by oligarchic growth, but the simplification is also inappropriate then. Therefore, two representative objects are introduced in the calculation after planetesimal formation: the massive object and less massive object. The massive object stirs the less massive object by gravitational perturbation and regulates the velocity dispersion or relative velocity between the massive and less massive objects. The scale height of the particle sub-disk H_p and the particle mass density in space ρ_p are also influenced by this stirring. Kokubo and Ida (2012) gave the mass evolution rate of the massive object in such a situation. Thus, we replace equation (7) with the mass evolution rate after the gravitational instability. Note that the massive object is the planetesimal and less massive objects are the

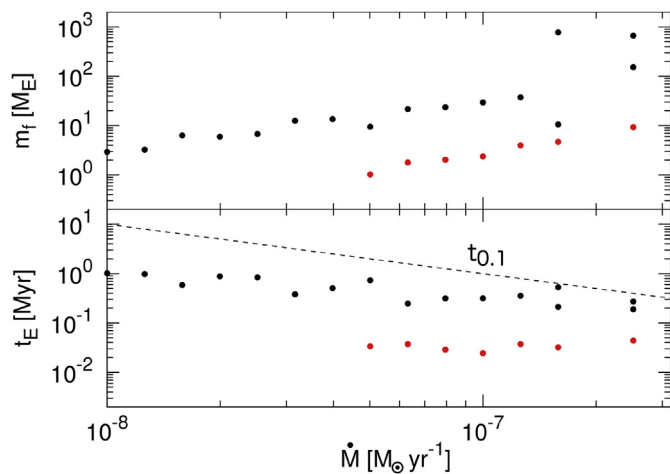


Figure 11. Same as Fig. 10 but for $B_z(100\text{AU}) = 3.4 \times 10^{-3} \text{ G}$. When both the black and red points coexist at the same accretion rate, this implies that tandem planet formation takes place. This occurs in the \dot{M} range of $10^{-7.3} - 10^{-6.4} M_{\odot} \text{ yr}^{-1}$.

remaining pebbles, which hold the mass just before the gravitational instability of the particle sub-disk.

All of these evolution equations are related each other nonlinearly and are numerically solved by iteration. For the detailed calculation, see paper I.

3.2. Results

Figs. 7–9 represent the particle growth in a disk with an accretion rate of $\dot{M} = 10^{-7.0} M_{\odot} \text{ yr}^{-1}$. The strengths of the magnetic field at 100 AU are $B_z(100\text{AU}) = 3.4 \times 10^{-3} \text{ G}$ (Fig. 7), $B_z(100\text{AU}) = 3.4 \times 10^{-4} \text{ G}$ (Fig. 8, canonical case in paper I), and $B_z(100\text{AU}) = 3.4 \times 10^{-5} \text{ G}$ (Fig. 9). All of the other parameters are the same as those in paper I.

As indicated in the previous section, the magnetic field only affects the locations of the MRI fronts. Therefore, the particle evolution is almost the same when the particles are far from the MRI fronts. Moreover, the location of the inner MRI front has a weak dependence on the magnetic field (Fig. 4) because it is dominantly determined by the thermal ionization condition, which is given by $T_m = 1000 - 1300 \text{ K}$. Based on the results, we can safely state that the particle evolution in the rocky region is the same in all three cases (see the red lines in Figs. 7–9).

On the other hand, the location of the outer MRI front changes drastically as a function of the magnetic field. In the cases of $B_z(100\text{AU}) = 3.4 \times 10^{-3} \text{ G}$ and $B_z(100\text{AU}) = 3.4 \times 10^{-4} \text{ G}$, the tandem planet formation regime holds up well. In other words, the super-particles originally located outside the outer MRI front drift inward to merge with the super-particles around the outer MRI front. The continuous inflow accelerates the particle growth, and the planets reach the Earth mass within $t_{0,1}$. This timescale of $t_{0,1}$ is the actual upper limit of the duration for a given accretion rate because the accretion mass $\dot{M} \times t_{0,1}$ exceeds $0.1 M_{\odot}$ after $t_{0,1}$, and the mass of the central star changes considerably.

However, for the case of $B_z(100\text{AU}) = 3.4 \times 10^{-5} \text{ G}$, the situation completely changes. First, the outer MRI front shifts beyond 100 AU, and the growth does not accelerate. Instead, the particles in the different super-particles grow independently, but the evolution speed is relatively slow. As a result, they do not reach the Earth mass (Fig. 9).

Figs. 14–16 show the planetary growth in the disk with the accretion rate of $\dot{M} = 10^{-7.5} M_{\odot} \text{ yr}^{-1}$. The strengths of the magnetic field are $B_z(100\text{AU}) = 3.4 \times 10^{-3} \text{ G}$, $B_z(100\text{AU}) = 3.4 \times 10^{-4} \text{ G}$, and $B_z(100\text{AU}) = 3.4 \times 10^{-5} \text{ G}$. Tandem planet formation actively takes place in the canonical (Fig. 15) and strongly magnetized cases (Fig. 14). However, it does not occur for the weakly magnetized disk (Fig. 16). Instead, a new regime of planetary formation emerges. In other words, the particles in the icy MSR independently grow without merging and successfully arrive at the Earth mass. We call this regime dispersed planet formation in contrast to tandem planet formation, where the planet formation is strictly restricted to the outer and inner MRI fronts.

4. Discussion

4.1. Solid mass distribution in the gas disk

We showed that tandem planet formation acts as a growth accelerator of planet formation that is strictly localized around the MRI fronts. Therefore, the location of the MRI front is particularly important for tandem planet formation. Fig. 4 shows the locations of the MRI fronts as a function of the strength of the magnetic field. The bottom panel in Fig. 10 shows the time when the particle reaches 1 Earth mass M_{\oplus} for the case of $B_z(100\text{AU}) = 3.4 \times 10^{-5} \text{ G}$. The dashed line represents $t_{0,1}$, which is the actual upper limit of the

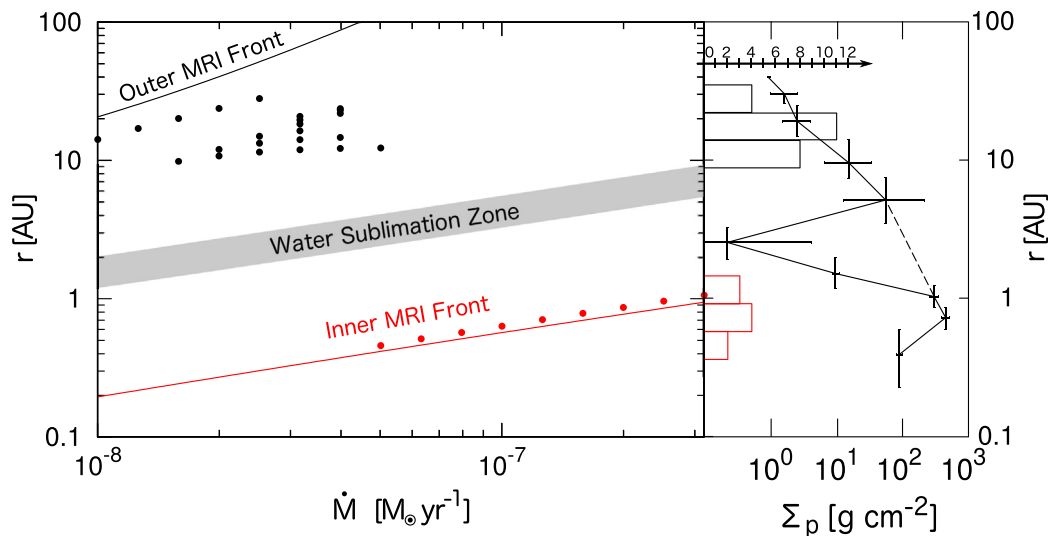


Figure 12. The left panel shows the final particle locations as a function of the accretion rate. The strength of the magnetic field at 100 AU is 3.4×10^{-5} G. Only the locations where the particle grows to $1M_{\oplus}$ within $t_{0.1}$ are plotted. The solid lines are the locations of the outer MRI front (black) and inner MRI front (red). The histogram in the right panel represents the number of points in each radius bin in the left panel. This indicates that it is difficult for a planet larger than $1M_{\oplus}$ to form between 2 AU and 8 AU (planet formation gap) in the gas disk with $B_z(100\text{AU}) = 3.4 \times 10^{-5}$ G. The solid line in the right panel is the estimated solid mass distribution of our present Solar System (Weidenschilling, 1977b), which was scanned from the original figure and rotated 90° for comparison. The gap between the rocky and icy planets is a bit too wide in this case.

duration for a given accretion rate, as stated in the previous section. Therefore, only the points below the dashed line are plotted. Calculations were performed from $\dot{M} = 10^{-6.5} M_{\odot} \text{ yr}^{-1}$ down to $\dot{M} = 10^{-8.0} M_{\odot} \text{ yr}^{-1}$ with a difference of 0.1 Dex. The black points represent the particles in the icy region, while the red points are those in the rocky region. When multiple particles acquire $\geq M_{\oplus}$, they are plotted at the same accretion rate. The top panel in Fig. 10 shows the final mass of the particle, which is defined by $m_f = 2\pi r_p r_H \Sigma_p$. Here, r_H and Σ_p are the particle Hill radius and particle column density, respectively. Fig. 11 is same as Fig. 10 but for $B_z(100\text{AU}) = 3.4 \times 10^{-3}$ G. Comparing these two figures shows that tandem planet formation takes place in the strong magnetic case.

The left panel in Fig. 12 shows the final particle locations from the central star. The strength of the magnetic field at 100 AU is

3.4×10^{-5} G. Only the locations, where the particle can grow to $1M_{\oplus}$ within $t_{0.1}$ are plotted. The histogram in the right panel represents the number of points in each radius bin in the left panel. The solid line in the right panel represents the estimated solid mass distribution of our present Solar System from Weidenschilling (1977b). This histogram shows that there is a region where no values are counted between the outer black pointed and inner red pointed region. This indicates that there is the planet formation gap between 2 to 8 AU in the gas disk with $B_z(100\text{AU}) = 3.4 \times 10^{-5}$ G. It is too wide compared with the gap observed in the solid component of the present Solar System.

Fig. 13 shows the same results but for $B_z(100\text{AU}) = 3.4 \times 10^{-3}$ G. The planet formation gap shrinks down to 2–4 AU and is consistent with the gap observed in the solid material of our present Solar System.

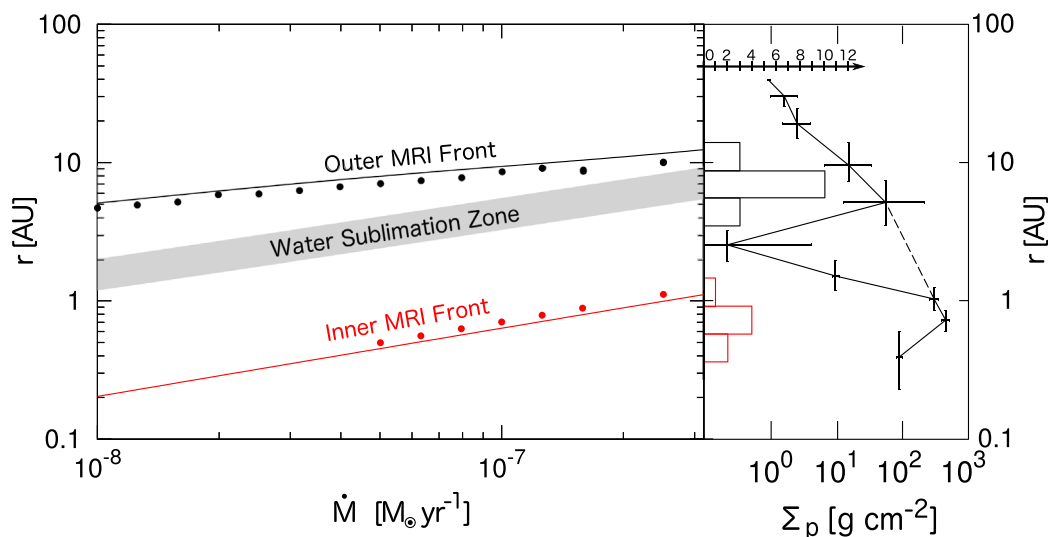


Figure 13. Same as Fig. 12 but for $B_z(100\text{AU}) = 3.4 \times 10^{-3}$ G. Tandem planet formation can be observed in the \dot{M} range between $10^{-7.3}$ and $10^{-6.4} M_{\odot} \text{ yr}^{-1}$. The planet formation gap shrinks to 2–4 AU, which is consistent with the present solid mass distribution of our Solar System.

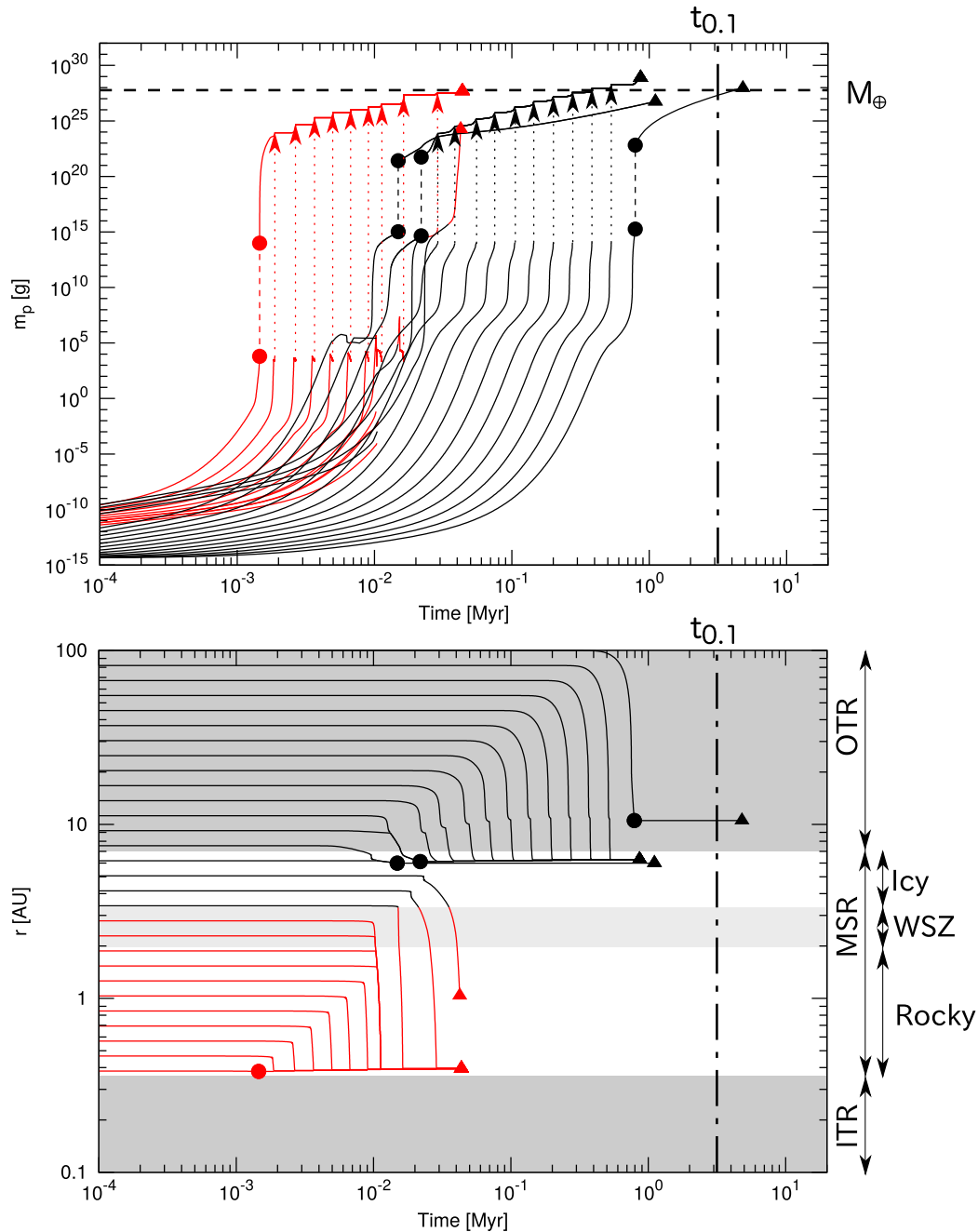


Figure 14. Same as Fig. 7 but for $\dot{M} = 10^{-7.5} M_{\odot} \text{ yr}^{-1}$ and $B_z(100\text{AU}) = 3.4 \times 10^{-3} \text{ G}$.

4.2. Tandem planet formation regime in strongly magnetized disk

As shown in Figs. 11 and 13, tandem planet formation holds up well in the strongly magnetized disk ($B_z = 3.4 \times 10^{-3} \text{ G}$) and in the canonical case ($B_z = 3.4 \times 10^{-4} \text{ G}$). The solid particles or pebbles accumulate into two distinct sites (i.e., the outer and inner MRI fronts), and the growth at other places is rare. Because of the continuous supply of pebbles into the formation sites, the planetary system is likely to be made of smaller numbers of larger planets (Levison et al., 2015) with relatively small orbital eccentricities.

4.3. Dispersed planet formation regime in weakly magnetized disk

Figs. 10 and 12 show a new regime of planet formation in the weakly magnetized disk ($B_z = 3.4 \times 10^{-5} \text{ G}$), where the planets grow

independently at different places in the dispersed area of the icy MRI-suppressed region of $r = 8\text{--}30 \text{ AU}$ when $\dot{M} = 10^{-7.8}\text{--}10^{-7.3} M_{\odot} \text{ yr}^{-1}$. A similar growth of planets is seen at a higher accretion rate, although they do not reach the Earth mass.

The outer MRI front recedes up to 70 AU when the magnetic field is as small as $B_z(100\text{AU}) = 3.4 \times 10^{-5} \text{ G}$ and $\dot{M} = 10^{-7.5} M_{\odot} \text{ yr}^{-1}$. The particles in the icy MSR grow through mutual sticking and begin to drift inward. However, because the particles have already been decoupled from the gas, the gravitational instability of the particle sub-disk takes place during the inward drift. Some of the planetesimals produced by this evolutionary path further grow and successfully reach the Earth mass within $t_{0.1}$. In sharp contrast to the tandem regime, the dispersed regime has a broad icy planet formation area that extends across 8–30 AU. In such a case, planets grow in different places eating nearby pebbles. As a result, a system

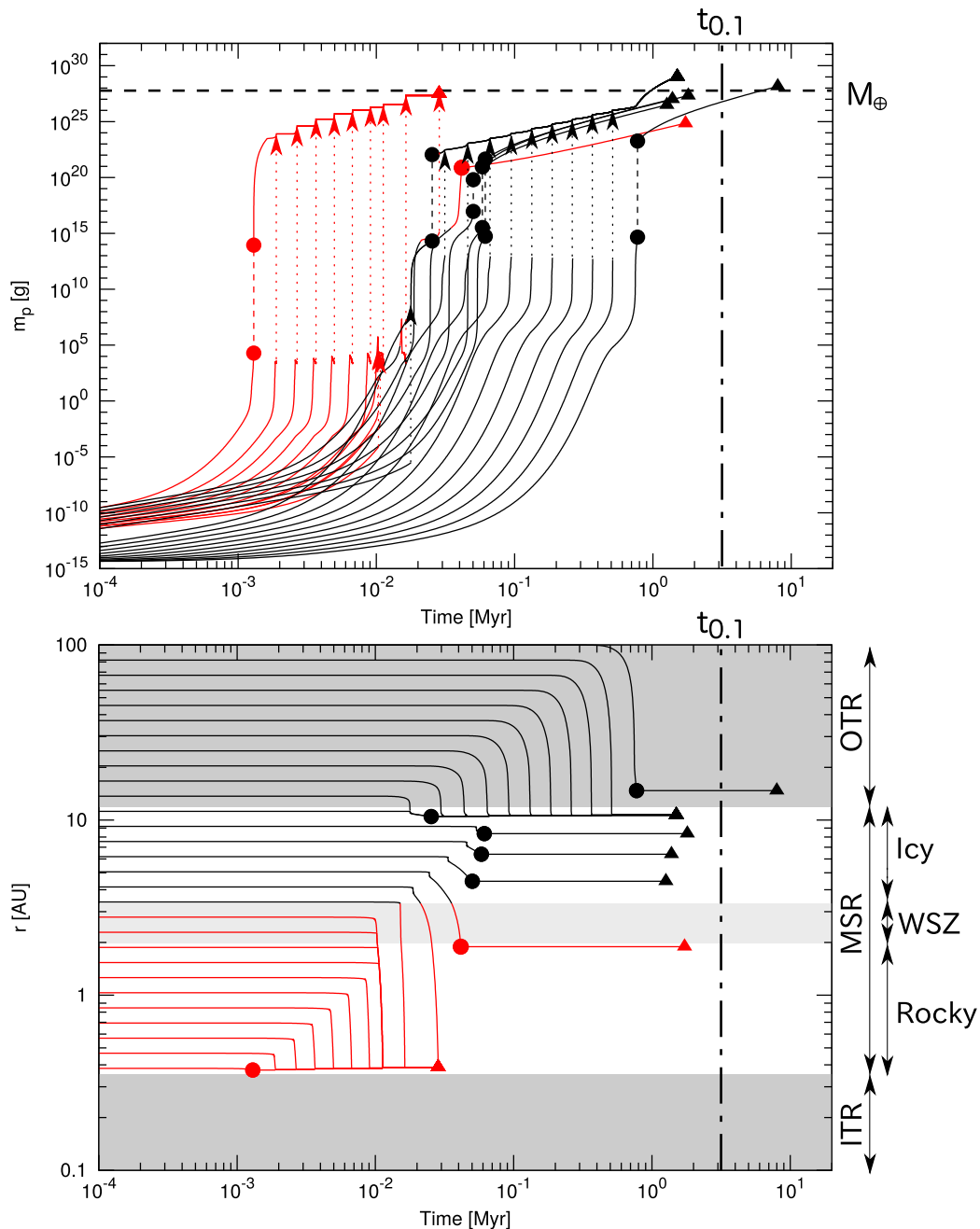


Figure 15. Same as Fig. 7 but for $\dot{M} = 10^{-7.5} M_{\odot} \text{ yr}^{-1}$ and $B_z(100\text{AU}) = 3.4 \times 10^{-4} \text{ G}$.

with a larger number of smaller planets is likely to develop (Levison et al., 2015). After the gas dissipation, the planets are strongly scattered among each other and grow through occasional giant impacts, and may become eccentric planets (Marcy and Butler, 1996), since the orbital eccentricities become high because of the gravitational scattering and catastrophic impacts. The final fate of such a system is still premature to discuss because of the simplified assumption of a one-dimensional disk. Intensive future works are needed.

4.4. Magnetic field in the inner part of the disk

As shown in Fig. 6, magnetic fields asymptotically converge with each other to 100 G at the innermost point of the disk (Alfvén radius

$\sim 0.02 \text{ AU}$), even if the strength of the magnetic field at 100 AU is different (Okuzumi et al., 2014). This value for the magnetic field is consistent with the observed photospheric magnetic field of protostars (Johns-Krull, 2007) if the gas contraction from $\sim 0.02 \text{ AU}$ to 0.01 AU is considered.

5. Conclusion and summary

We investigated the dependence of the magnetic field strength on the tandem planet formation model. We calculated two cases of $B_z(100\text{AU}) = 3.4 \times 10^{-3} \text{ G}$ and $B_z(100\text{AU}) = 3.4 \times 10^{-5} \text{ G}$ as well as the canonical case of $B_z(100\text{AU}) = 3.4 \times 10^{-4} \text{ G}$. We found the following:

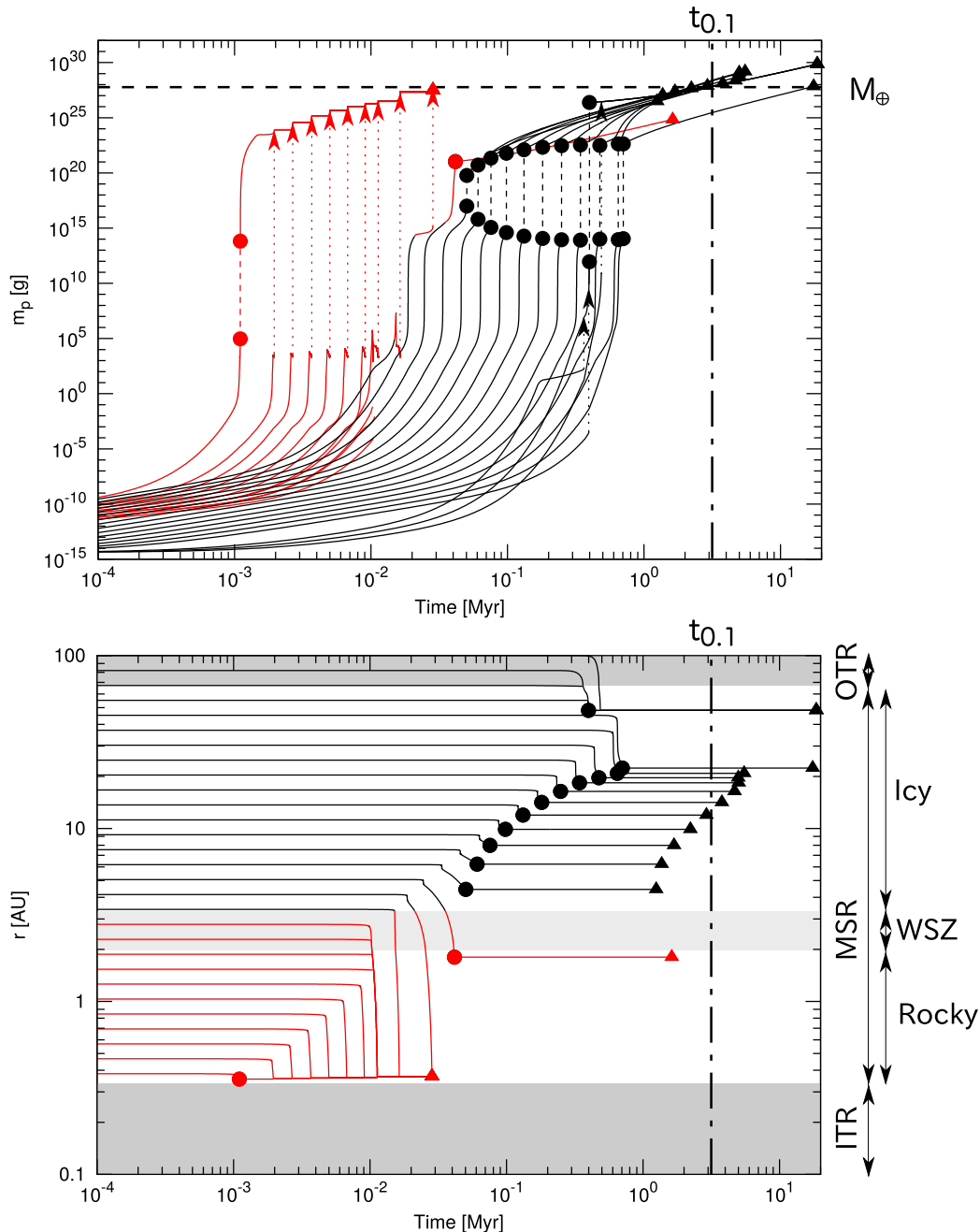


Figure 16. Same as Fig. 7 but for $\dot{M} = 10^{-7.5} M_{\odot} \text{ yr}^{-1}$ and $B_z(100\text{AU}) = 3.4 \times 10^{-5} \text{ G}$.

First, the tandem planet formation regime holds up well for the strong magnetic field $B_z(100\text{AU}) = 3.4 \times 10^{-3} \text{ G}$ and canonical cases. Solid particles are concentrated at both the outer and inner MRI fronts and form planetesimals there through the gravitational instability of the particle sub-disk. The planetesimals at the outer MRI front are the origin of the gas giant cores and icy planets, while the planetesimals at the inner MRI front are the terrestrial planets. The continuous radial inflow of the particles into the planet formation sites considerably accelerates the growth of the planetesimals and solves the growth timescale problem in the conventional planet formation theory. The particle drift also explains the deficit of the solid material between the two MRI fronts. The temperature of the inner MRI front is considerably above the sublimation temperature of H_2O but below the sublimation temperature of silicate

or olivine, which accounts for the formation of the volatile-free terrestrial planet. This meets the condition of the ABEL model proposed by Maruyama and Ebisuzaki (2016), in which the small amount of the volatile components (e.g. water) are added after the volatile-free planet forms first.

Second, for the case of the weak magnetic field $B_z(100\text{AU}) = 3.4 \times 10^{-5} \text{ G}$, a new regime of planet formation called dispersed planet formation takes place: the planets grow independently in different places in the dispersed area of the MSR of $r = 8\text{--}30 \text{ AU}$ at a lower accretion rate of $\dot{M} < 10^{-7.4} M_{\odot} \text{ yr}^{-1}$. This may lead to a system of a larger number of smaller planets. The planets in such a system develop large orbital eccentricities through strong gravitational scattering and giant impacts. Rocky planets that form in the inner part of the planetary system may

have too much water through numerous impacts of icy objects from outside the system, and this is inconsistent with the concept of the Habitable Trinity for the emergence of life on the planet proposed by Dohm and Maruyama (2015).

Acknowledgments

We thank Prof. S. Maruyama for his continuous encouragement. This work was partly supported by a Grant-in-Aid for Scientific Research on Innovative Areas (Grant No. 26106006).

References

- Armitage, P.J., 2011. Dynamics of protoplanetary disks. *Annual Review of Astronomy and Astrophysics* 49, 195–236.
- Balbus, S., Hawley, J., 2000. Solar nebula magnetohydrodynamics. *Space Science Reviews* 92 (1–2), 39–54.
- Balbus, S.A., Hawley, J.F., 1991. A powerful local shear instability in weakly magnetized disks. I – linear analysis. *The Astrophysical Journal* 376, 214–222.
- Bouvier, J., Alencar, S.H.P., Boutelier, T., Dougados, C., Balog, Z., Grankin, K., Hodgkin, S.T., Ibrahimov, M.A., Kun, M., Magakian, T. Yu., Pinte, C., 2007. Magnetospheric accretion-ejection processes in the classical t tauri star aa tauri. *Astronomy and Astrophysics* 463 (3), 1017–1028.
- Carballido, A., Fromang, S., Papaloizou, J., 2006. Mid-plane sedimentation of large solid bodies in turbulent protoplanetary discs. *Monthly Notices of the Royal Astronomical Society* 373, 1633–1640.
- Chatterjee, S., Tan, J.C., 2014. Inside-out planet formation. *The Astrophysical Journal* 780, 53.
- Chatterjee, S., Tan, J.C., 2015. Vulcan planets: inside-out formation of the innermost super-Earths. *The Astrophysical Journal Letters* 798, L32.
- Crutcher, R.M., Wandelt, B., Heiles, C., Falgarone, E., Troland, T.H., 2010. Magnetic fields in interstellar clouds from Zeeman observations: inference of total field strengths by Bayesian analysis. *The Astrophysical Journal* 725, 466–479.
- Dohm, J.M., Maruyama, S., 2015. Habitable trinity. *Geoscience Frontiers* 6 (1), 95–101.
- Ebisuzaki, T., Imaeda, Y., 2016. United Theory of Planet Formation (I): Tandem Regime (Paper I). *ArXiv e-prints*, 1601.05509.
- Gammie, C.F., 1996. Layered accretion in T Tauri disks. *The Astrophysical Journal* 457, 355.
- Goldreich, P., Ward, W.R., 1973. The formation of planetesimals. *The Astrophysical Journal* 183, 1051–1062.
- Hawley, J.F., Balbus, S.A., 1991. A powerful local shear instability in weakly magnetized disks. II. Nonlinear evolution. *The Astrophysical Journal* 376, 223–233.
- Hayashi, C., Nakazawa, K., Nakagawa, Y., 1985. Formation of the solar system. In: Black, D.C., Matthews, M.S. (Eds.), *Protostars and Planets II*, pp. 1100–1153.
- Hubeny, I., 1990. Vertical structure of accretion disks – a simplified analytical model. *The Astrophysical Journal* 351, 632–641.
- Imaeda, Y., Ebisuzaki, T., 2016. Tandem planet formation for solar-system like planetary systems (paper II). *Geoscience Frontiers* (in press). <http://dx.doi.org/10.1016/j.gsf.2016.06.011>.
- Jin, L., 1996. Damping of the shear instability in magnetized disks by Ohmic diffusion. *The Astrophysical Journal* 457, 798.
- Johansen, A., Klahr, H., Henning, T., 2006. Gravitational formation of planetesimals. *The Astrophysical Journal* 636, 1121–1134.
- Johansen, A., Klahr, H., Henning, T., 2011. High-resolution simulations of planetesimal formation in turbulent protoplanetary discs. *Astronomy & Astrophysics* 529, A62.
- Johansen, A., Lacerda, P., 2010. Prograde rotation of protoplanets by accretion of pebbles in a gaseous environment. *Monthly Notices of the Royal Astronomical Society* 404, 475–485.
- Johansen, A., Oishi, J.S., Mac Low, M.-M., Klahr, H., Henning, T., Youdin, A., 2007. Rapid planetesimal formation in turbulent circumstellar disks. *Nature* 448, 1022–1025.
- Johansen, A., Youdin, A., 2007. Protoplanetary disk turbulence driven by the streaming instability: nonlinear saturation and particle concentration. *The Astrophysical Journal* 662, 627–641.
- Johansen, A., Youdin, A., Mac Low, M.-M., 2009. Particle clumping and planetesimal formation depend strongly on metallicity. *The Astrophysical Journal Letters* 704, L75–L79.
- Johns-Krull, C.M., 2007. The magnetic fields of classical T Tauri stars. *The Astrophysical Journal* 664, 975–985.
- Kataoka, A., Tanaka, H., Okuzumi, S., Wada, K., 2013. Fluffy dust forms icy planetesimals by static compression. *Astronomy and Astrophysics* 557, L4.
- Kokubo, E., Ida, S., 1998. Oligarchic growth of protoplanets. *Icarus* 131, 171–178.
- Kokubo, E., Ida, S., 2012. Dynamics and accretion of planetesimals. *Progress of Theoretical and Experimental Physics* 2012 (1), 01A308.
- Kusaka, T., Nakano, T., Hayashi, C., 1970. Growth of solid particles in the primordial solar nebula. *Progress of Theoretical Physics* 44, 1580–1595.
- Lambrechts, M., Johansen, A., 2012. Rapid growth of gas-giant cores by pebble accretion. *Astronomy and Astrophysics* 544, A32.
- Lambrechts, M., Johansen, A., 2014. Forming the cores of giant planets from the radial pebble flux in protoplanetary discs. *Astronomy and Astrophysics* 572, A107.
- Lazarian, A., Vishniac, E.T., 1999. Reconnection in a weakly stochastic field. *The Astrophysical Journal* 517, 700–718.
- Levison, H.F., Kretke, K.A., Duncan, M.J., 2015. Growing the gas-giant planets by the gradual accumulation of pebbles. *Nature* 524, 322–324.
- Lynden-Bell, D., Pringle, J.E., 1974. The evolution of viscous discs and the origin of the nebular variables. *Monthly Notices of the Royal Astronomical Society* 168, 603–637.
- Marcy, G.W., Butler, R.P., 1996. A planetary companion to 70 virginis. *The Astrophysical Journal Letters* 464, L147.
- Maruyama, S., Ebisuzaki, T., 2016. Origin of the earth: a proposal of new model called abel. *Geoscience Frontiers* (Submitted).
- Mizuno, H., 1980. Formation of the giant planets. *Progress of Theoretical Physics* 64, 544–557.
- Nakagawa, Y., Sekiya, M., Hayashi, C., 1986. Settling and growth of dust particles in a laminar phase of a low-mass solar nebula. *Icarus* 67, 375–390.
- Okuzumi, S., Takeuchi, T., Muto, T., 2014. Radial transport of large-scale magnetic fields in accretion disks. I. Steady solutions and an upper limit on the vertical field strength. *The Astrophysical Journal* 785, 127.
- Okuzumi, S., Tanaka, H., Kobayashi, H., Wada, K., 2012. Rapid coagulation of porous dust aggregates outside the snow line: a pathway to successful icy planetesimal formation. *The Astrophysical Journal* 752, 106.
- Ormel, C.W., Cuzzi, J.N., 2007. Closed-form expressions for particle relative velocities induced by turbulence. *Astronomy and Astrophysics* 466, 413–420.
- Ormel, C.W., Klahr, H.H., 2010. The effect of gas drag on the growth of protoplanets. Analytical expressions for the accretion of small bodies in laminar disks. *Astronomy and Astrophysics* 520, A43.
- Paardekooper, S.-J., 2014. Dynamical corotation torques on low-mass planets. *Monthly Notices of the Royal Astronomical Society* 444, 2031–2042.
- Pollack, J.B., Hubickyj, O., Bodenheimer, P., Lissauer, J.J., Podolak, M., Greenzweig, Y., 1996. Formation of the giant planets by concurrent accretion of solids and gas. *Icarus* 124, 62–85.
- Ruden, S.P., Pollack, J.B., 1991. The dynamical evolution of the protosolar nebula. *The Astrophysical Journal* 375, 740–760.
- Safronov, V.S., 1969. Evolution of the Protoplanetary Cloud and Formation of the Earth and the Planets. Nauka, Moscow (translated by Israel program for scientific translations, Keter press, Jerusalem. (Also by NASA TTF-677).
- Sano, T., Miyama, S.M., 1999. Magnetorotational instability in protoplanetary disks. I. On the global stability of weakly ionized disks with ohmic dissipation. *The Astrophysical Journal* 515, 776–786.
- Sano, T., Miyama, S.M., Umebayashi, T., Nakano, T., 2000. Magnetorotational instability in protoplanetary disks. II. Ionization state and unstable regions. *The Astrophysical Journal* 543, 486–501.
- Sasaki, T., Ebisuzaki, T., 2016. Population synthesis of planet formation using a torque formula with dynamic effects. *Geoscience Frontiers* (in press). <http://dx.doi.org/10.1016/j.gsf.2016.04.002>.
- Sato, T., Okuzumi, S., Ida, S., 2016. On the Water Delivery to Terrestrial Embryos by Ice Pebble Accretion. *Astronomy and Astrophysics* 589, A15.
- Shakura, N.I., Sunyaev, R.A., 1973. Black holes in binary systems. Observational appearance. *Astronomy and Astrophysics* 24, 337–355.
- Stepinski, T.F., 1998. The solar nebula as a process-analytic model. *Icarus* 132, 100–112.
- Stewart, S.T., Leinhardt, Z.M., 2009. Velocity-dependent catastrophic disruption criteria for planetesimals. *The Astrophysical Journal Letters* 691, L133–L137.
- Takeuchi, T., Muto, T., Okuzumi, S., Ishitsu, N., Ida, S., 2012. Induced turbulence and the density structure of the dust layer in a protoplanetary disk. *The Astrophysical Journal* 744, 101.
- Turner, N.J., Sano, T., Dziourkevitch, N., 2007. Turbulent mixing and the dead zone in protostellar disks. *The Astrophysical Journal* 659, 729–737.
- Umebayashi, T., Nakano, T., 1988. Ionization state and magnetic fields in the solar nebula. *Progress of Theoretical Physics Supplement* 96, 151–160.
- Wada, K., Tanaka, H., Suyama, T., Kimura, H., Yamamoto, T., 2009. Collisional growth conditions for dust aggregates. *The Astronomical Journal* 702 (2), 1490–1501.
- Weidenschilling, S., 1977b. The distribution of mass in the planetary system and solar nebula. *Astrophysics and Space Science* 51 (1), 153–158.
- Weidenschilling, S.J., 1977a. Aerodynamics of solid bodies in the solar nebula. *Monthly Notices of the Royal Astronomical Society* 180, 57–70.
- Weidenschilling, S.J., Cuzzi, J.N., 1993. Formation of planetesimals in the solar nebula. In: Levy, E.H., Lunine, J.I. (Eds.), *Protostars and Planets III*, pp. 1031–1060.
- Wetherill, G.W., Stewart, G.R., 1989. Accumulation of a swarm of small planetesimals. *Icarus* 77, 330–357.
- Yamoto, F., Sekiya, M., 2004. The gravitational instability in the dust layer of a protoplanetary disk: axisymmetric solutions for nonuniform dust density distributions in the direction vertical to the midplane. *Icarus* 170, 180–192.
- Youdin, A.N., Lithwick, Y., 2007. Particle stirring in turbulent gas disks: including orbital oscillations. *Icarus* 192, 588–604.